

The Influence of Minority Carrier Density on Degradation and Regeneration Kinetics in Multicrystalline Silicon Wafers

Guro Marie Wyller , Marie Syre Wiig , Ida Due-Sørensen , and Rune Søndena 

Abstract—The rate at which silicon solar cells and wafers degrade and regenerate when subjected to light and elevated temperatures (LeTID) is known to depend on the minority carrier concentration. In this article, we utilize spatial differences in the rate of degradation and regeneration in multicrystalline silicon wafers to estimate the dependence of these rates on minority carrier concentration. We apply the relation obtained from spatial investigations in a model describing temporal LeTID defect evolution. With the updated model in which the evolving minority charge carrier density during degradation and regeneration is considered, we obtain a drastically improved fit between measured and modeled data. The activation energy for the regeneration process determined from our proposed model (0.56 ± 0.12 eV at 1 sun) is lower than most values reported in the literature but correspond perfectly to the activation energy reported by Graf *et al.* by whom evolving carrier injection is accounted for experimentally. Hence, our results underpin the importance of taking the evolution of charge carrier injection into account in the evaluation of LeTID kinetics. Finally, we use our updated model to obtain spatial maps of degradation and regeneration parameters. Clear correlations are shown between LeTID kinetics parameters and local processing conditions.

Index Terms—Charge carrier density, defect reactions, degradation, light- and elevated temperature-induced degradation (LeTID), modeling.

I. INTRODUCTION

DEGRADATION of minority charge carrier lifetime, or *lifetime* for short, in solar cells and wafers induced by light and elevated temperature, often denoted LeTID [1], was first reported by Ramspeck *et al.* [2] in 2012 in p-type mc-Si PERC solar cells. Despite an intensive research effort to identify and understand the defect mechanism, the root cause of LeTID is still not fully understood. The involvement of hydrogen (H) is, however, strongly suspected ([3]–[10]).

Various models have been proposed to describe the lifetime evolution in solar cells subjected to light at elevated temperatures. First, a 3-state model, originally developed for the

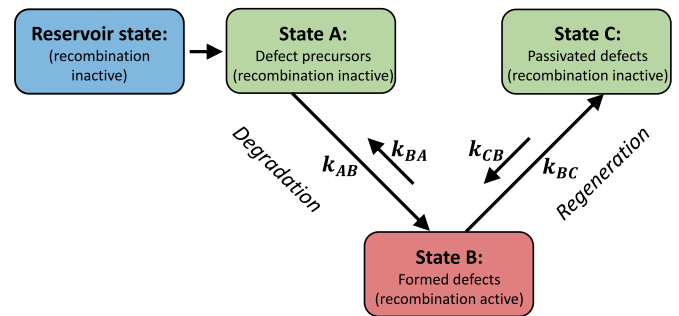


Fig. 1. Proposed four-state model for the LeTID defect system, after Fung *et al.* [12]. Arrows represent possible transitions between the defect states. Figure adapted from Kwapil *et al.* [15].

boron-oxygen-(BO)-related degradation and regeneration was adopted to account for the LeTID related degradation and regeneration process [11]. The 3-state model assumes that after firing most LeTID defects are in an *inactive precursor state A* allowing for a high carrier lifetime. Upon carrier injection and heat treatment, the system moves into the *recombination active state B*, causing significantly reduced lifetime. After prolonged treatment at degradation conditions, the system moves further into the *regenerated state C* in which the LeTID defects are deactivated, again allowing high carrier lifetimes. The model has later been expanded to a four-state-model [12], including a *reservoir state* from which state A precursors can be replenished. Fig. 1 illustrates the four states: *reservoir*, A, B, and C as well as the transitions between them. As indicated by the arrows in the figure, the transitions from A to B and from B to C are assumed to be reversible, whereas the transition from the reservoir state to A is assumed to be irreversible [12].

It has been shown that repeated light-soaking and dark annealing (DA) treatment can cause multiple degradation and regeneration cycles [12]–[14]. By such cycling, however, the degradation extent gradually decreases, indicating the depletion of the reservoir by an irreversible transition from the reservoir state to state A [12]. Hence, the lifetime variations resulting from DA/LeTID cycling can mainly be considered as the movement of defects from the reservoir state via state A and B to state C. On the other hand, it has recently been shown that the transition from the recombination active defect B back to the precursor state A can happen under carrier injection at room temperature [15]. This transition, denoted temporary recovery, as well as the transition

Manuscript received February 2, 2021; revised March 10, 2021 and April 17, 2021; accepted April 27, 2021. Date of publication May 27, 2021; date of current version June 21, 2021. This work was supported by the Norwegian Research Council through the projects LeTID in multicrystalline PERC cells (280909) and Erasing the detrimental structural defects in multicrystalline silicon wafers (296309). (Corresponding author: Rune Søndena.)

The authors are with the Institute of Energy Technology, 2027 Kjeller, Norway (e-mail: g.m.wyller@gmail.com; marie.syre.wiig@ife.no; ida.due.s@gmail.com; rune.sondena@ife.no).

Color versions of one or more figures in this article are available at <https://doi.org/10.1109/JPHOTOV.2021.3078367>.

Digital Object Identifier 10.1109/JPHOTOV.2021.3078367

2156-3381 © 2021 IEEE. Personal use is permitted, but republication/redistribution requires IEEE permission. See <https://www.ieee.org/publications/rights/index.html> for more information.

back to the degraded state B, can happen repeatedly with very little change in the degraded and recovered state between the cycles [15]. It is therefore interpreted as a reversible alternation between two equilibrium states, controlled by changes in temperature and injection conditions [15]. In the context of this work, it is most relevant to note that the overall LeTID dynamics seem to be governed by the complex interactions between four defect states [12], we can—depending on conditions—focus on only some of the transitions between these states. In the rest of this work, our focus will be on states A, B, and C.

A. Kinetic Description of Degradation and Regeneration

The rate R of a chemical reaction is normally assumed to scale with the concentration of the reacting species according to the relation

$$R = k[P]^p[Q]^q \quad (1)$$

where $[P]$ and $[Q]$ are the concentrations of the reacting species and p and q are their stoichiometric coefficients in the reaction. The constant k is the reaction *rate coefficient*, normally assumed to be governed by the Arrhenius equation, given by

$$k = A \cdot e^{-E_a/k_B T} \quad (2)$$

in which E_a is the activation energy of the reaction, T is the present absolute temperature, k_B is Boltzmann's constant and A is a pre-exponential factor often denoted the *attempt frequency* of the reaction.

The overall rate of a reversible reaction is the difference between the forward and the backward reaction rates. Assuming that the transitions between the states A, B, and C (sketched in Fig. 1) are first order with respect to the involved species, we can express the rate of change of the recombination active defect B as follows:

$$\begin{aligned} \frac{\partial N_B(t)}{\partial t} = & (k_{AB}N_A(t) - k_{BA}N_B(t)) \\ & + (k_{CB}N_C(t) - k_{BC}N_B(t)). \end{aligned} \quad (3)$$

Here, the first bracket represents the degradation, and the second bracket represents the subsequent regeneration process. The number $N_i(t)$ represent the concentration of each state ($i = A, B$, or C), while k_{ij} represent the rate constant from state i to j (after [12]).

The presence of excess carriers is shown to influence degradation and regeneration rates [12], [16]–[18], and it is therefore reasonable to assume that charge carriers play a role in the reaction [19], [20]. One may regard charge carriers as a reacting species in these processes, and hence, express the degradation and regeneration rates as a function of the excess carrier density Δn , in line with (1). This would imply that also (3) should contain terms including Δn .

Kwapil *et al.* [16] have shown that the rate of degradation during LeTID varies almost linearly with the excess carrier density at the pn-junction for low and intermediate injection levels. Hence, they suggest that charge carriers are limiting to the degradation process. The regeneration is also shown to set in earlier in regions of high initial lifetime [21], [22] an indication

that the process might be accelerated by charge carriers. The aim of this work is to quantify the effect of excess charge carrier density on LeTID kinetics.

B. Simplifications Using the Normalized Defect Density

The number $N_B(t)$ in (3) is the actual concentration of activated defects given in units of cm^{-3} . Since the physical and chemical nature of the defect to date is unknown, this concentration is hard to measure or estimate [15]. In most experimental studies, one is therefore left with normalized defect density $\text{NDD}(t)$, given in units of s^{-1} . This quantity is defined as

$$\text{NDD}(t) = \frac{1}{\tau_{\text{effective}}} - \frac{1}{\tau_0} \quad (4)$$

where τ_0 and $\tau_{\text{effective}}(t)$ represent the initial effective lifetime and the effective lifetime at time t , respectively, [23]. The evolution with time of $\text{NDD}(t)$ will in many cases give a good indication of the evolution with time of the actual active defect concentration $N_B(t)$. One must, however, keep in mind that their units and therefore their absolute values will differ. Moreover, any defect causing the effective lifetime to change with time will contribute to the calculated value $\text{NDD}(t)$. For example, a contribution to $\text{NDD}(t)$ from BO-related degradation, which might be alleviated by testing LeTID with DA [22], must be expected in high performance multicrystalline silicon (HPMC-Si) wafers, [24], [25]. Despite these drawbacks, using NDD as an indication for the amount of recombination active defects give valuable information on the defect evolution and allow for mathematical descriptions of the process in lieu of more exact chemical descriptions.

The single-exponential function

$$\text{NDD}(t) = \text{NDD}_{\text{max}} (1 - e^{-R_{\text{deg}} t}) \quad (5)$$

has been used to fit the first part of the degradation curve, before regeneration sets in [26]. Here, NDD_{max} is the maximum value of NDD and R_{deg} is the degradation rate. Comparing this expression with the rate equation in (3), we note that the variable R_{deg} in (5) incorporates the entire term $k_{AB}N_A(t) - k_{BA}N_B(t)$ from (3). Using the approximation in (5), it must therefore be considered that both N_A and N_B likely will change during the degradation process. It has been shown that a better fit can be obtained using a sum of two exponentials to represent the degradation process [6], [27]. This approach can partly account for changes in N_A and N_B during the process.

Vargas *et al.* [18] have proposed a model describing both the degradation and the subsequent regeneration of the lifetime by the sum of two exponential functions

$$\text{NDD}(t) = \text{NDD}_{\text{max}} \{ [1 - e^{-R_{\text{deg}} t}] - (1 + A) [1 - e^{-R_{\text{reg}} t}] \}. \quad (6)$$

In this model R_{deg} and R_{reg} represent the degradation and regeneration rates, respectively. A potential deviation between the regenerated lifetime and the initial lifetime is reflected by the constant A . This model accounts for the fact that degradation and regeneration may occur simultaneously. Regeneration of the lifetime may very well commence before complete degradation

is achieved especially, for elevated temperatures [16], [18]. In addition, in this case, it must be kept in mind that R_{deg} and R_{reg} are empirical fitting constants, incorporating several terms from the chemical rate equation [see (3)]. In this work, we will apply (6) as starting point for further kinetic evaluations and for spatial mapping of degradation parameters.

C. Spatial Differences in Light and Elevated Temperature-Induced Degradation Kinetics

Several authors have investigated the spatial evolution of LeTID in multicrystalline silicon. Lower degradation extent has been reported close to grain boundaries and has been attributed to the formation of denuded zones formed by internal gettering of the LeTID defect [13], [26], [28]–[30]. On the other hand, it has been shown that the degradation occurs first in low-lifetime regions [10] and that the relative lifetime change caused by degradation is stronger in regions of poor initial quality, i.e., in regions limited by crystal defects such as grain boundaries, dislocation clusters, and precipitates [21]. Both these observations were done in gettered samples [10], [21].

Slight differences in processing conditions have been pointed out as an important reason for spatial differences in LeTID behavior [10], [26], [31], [32]. Especially, a strong influence is observed from the firing temperature and the firing temperature ramp [19], [33], [34]. The spatial distribution of LeTID defect density is shown to correspond to the pattern of the furnace belt or pins carrying the wafer during the fast firing step [26], [32].

As was already touched upon in Section I-A, the presence of excess carriers is assumed to influence the degradation and regeneration rates [12], [16]–[18]. As the charge carrier density vary spatially, especially in multicrystalline material, this influence will also cause degradation and regeneration rates to vary spatially. For example, the regeneration process is shown to set in earlier in regions of high initial lifetime [21], [22]. Fast recovery of high lifetime regions compared with lower lifetime regions is observed also in boron-doped float zone silicon [35]. In a wedge-shaped wafer, it has been shown that the regeneration of the lifetime proceeds at a faster rate in the thinner areas than in thicker areas [36], also pointing to an acceleration of the process upon increased excess carrier density. A recent study by Varshney *et al.* [37] has shown a direct correlation between wafer thickness and LeTID degradation extent. The authors explain the reduced degradation in thinner wafers with an increase in hydrogen effusion per unit volume during firing. As opposed to Bredemeier *et al.* [7], [36], these authors [37] found R_{deg} and R_{reg} to be independent of wafer thickness, possibly suggesting that these rates are not depending on carrier injection. It should be noted, however, that the results by Varshney *et al.* [37] were obtained at very high illumination (~ 54 suns), which likely could lead to saturation effects covering the influence of charge carrier injection on the degradation and regeneration rates.

In this work, we present a detailed investigation on the effect of excess charge carrier density on degradation and regeneration kinetics. We utilize the spatial differences in charge carrier density in our HPMC-Si wafers as well as differences caused by varied illumination intensity to extract the injection dependence

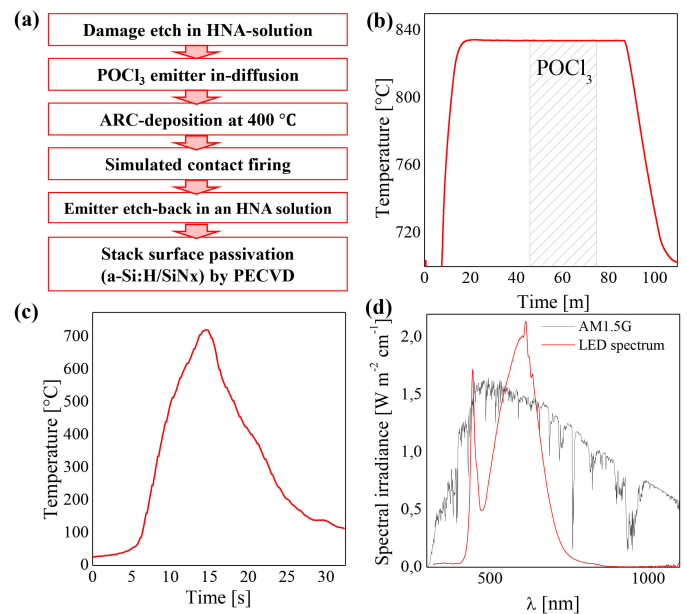


Fig. 2. (a) Sketch of the process flow to which the samples were subjected. (b) Process temperature during the emitter in-diffusion process, resulting in a sheet resistance of ca. $70 \Omega/\text{sq}$. (c) Temperature profile during the simulated contact firing step. The firing was performed without the metal contacts present. (d) LED-spectrum emitted by the light soaker (appr. 0.4 suns), compared with the AM1.5G reference spectrum.

of the degradation and regeneration rates. Further, we apply these dependencies in an improved mathematical description of the degradation and regeneration processes. Finally, we obtain spatially resolved maps of degradation and regeneration parameters.

II. EXPERIMENTAL DETAILS

A. Sample Preparation

Sister wafers from approximately 40% height of a corner brick from a commercially available p-type high performance multicrystalline (HPMC) Si ingot were chosen for this study. The ingot consisted of compensated silicon material in which the resistivity profile was engineered using tri-doping including boron, phosphorus and gallium, giving a resistivity of about $0.7 \Omega\cdot\text{cm}$. The investigated wafers were about $180 \mu\text{m}$ thick.

The process flow to which the wafers were subjected is designed to produce samples for lifetime measurements with a surface recombination velocity (SRV) of less than 5 cm/s [38]. The processing steps are listed schematically in Fig. 2(a). Wafers were first treated in an HNA solution (hydrofluoric, nitric, and acetic acid) to remove saw-damage. Thereafter, two-sided emitters were created by a POCl_3 in-diffusion process [see Fig. 2(b)]. Subsequently, SiN_x ARC layers were deposited on both sides of the wafers using PECVD. Hydrogenation was achieved with a simulated contact firing step [T_{peak} of about 725°C , see Fig. 2(c)] in a belt furnace. The hydrogenation process is confirmed in ref. [39], using Fourier transform infrared absorption spectroscopy (FT-IR) on similarly processed wafers. Finally, the SiN_x layer and the emitter layer were etched away, and

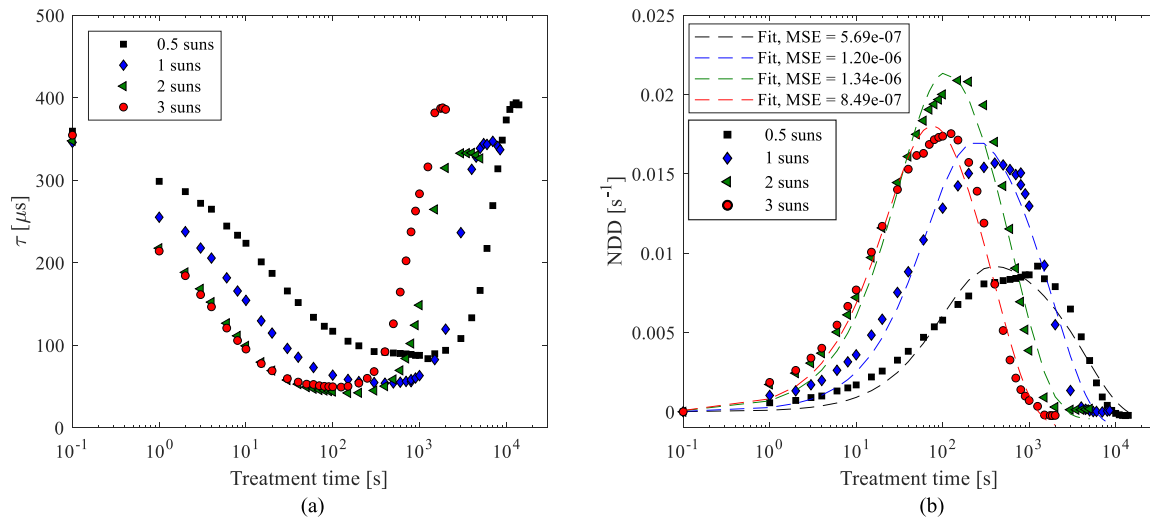


Fig. 3. (a) Lifetime development and (b) development of NDD as function of treatment time of mc-Si wafers treated at 150 °C with various illumination intensity. The lifetime and NDD values are calculated as an average over the central part of our PL images, corresponding to the QSSPC measurement coil. Pane (b) also include least square approximation (dashed lines) of the equation suggested by Vargas *et al.* [18] [see (6)] to our experimental data. The quality of the fit, quantified by its mean square error (MSE) is indicated in the legend.

the wafers were repassivated with an amorphous silicon/silicon nitride (a-Si/SiN_x) stack, deposited using PECVD.

B. Light- and Elevated Temperature Treatment

Twelve 5 cm × 5 cm sister tokens were laser cleaved from the processed wafers and subjected to LeTID-treatment, i.e., illuminated annealing, with different combinations of temperature and light intensity. Temperatures in the range 125 °C–175 °C and illumination intensities in the range 0.5–3 suns were used. The LeTID treatment was conducted using a LED-based light soaking system from Wavelabs, equipped with an integrated hotplate. The spectrum emitted by the light soaking system differs from the solar reference spectrum [see Fig. 2(d)]. To account for this, the illumination intensities were calculated based on the flux density in the wavelength range 320–1100 nm, which is the relevant range for charge carrier excitation in silicon. Thus, the unit “1 sun” here refers to a light intensity giving a photon flux in the wavelength range 320–1100 nm equivalent to that of the ASTM G173 spectrum, i.e., 2.7×10^{17} photons/(cm²·s). With this definition, and assuming a wafer thickness of 175 μm and 10% reflection, the 1 sun equivalent generation rate amounts to $1.4 \times 10^{19} \text{ cm}^{-3} \cdot \text{s}^{-1}$.

C. Lifetime Measurements

The minority carrier lifetime was periodically measured during the annealing treatment using a quasi-steady-state photoconductance (QSSPC)-calibrated photoluminescence (PL) imaging setup (LIS-R1 from BTI) at room temperature. At each measurement point, we obtain spatially resolved maps ($\sim 300 \times 300$ pixels) of the charge carrier lifetime. The QSSPC lifetimes were extracted at an injection level of $\Delta n \approx 0.1 \cdot p_0$ where p_0 is the thermal equilibrium concentration of holes. This corresponds to an injection of approximately $2.2 \cdot 10^{15} \text{ cm}^{-3}$. The PL-images

were captured using a constant generation rate. All measurements were conducted by manual movement of the sample between the light soaker and the PL imaging setup. Fig. 10 in the appendix displays injection dependent lifetime curves for the wafer degraded at 150 °C and with 1 Sun illumination in its initial, degraded and regenerated state, along with equivalent lifetime curves for 0.5, 1, 2, and 3 suns.

III. RESULTS AND DISCUSSION

A. Evolution of Normalized Defect Density During Illumination and Heat Treatment

The lifetime evolution, of samples annealed at 150 °C with different illumination intensities are displayed in Fig. 3(a). As expected, we observe that the lifetimes first decrease relatively fast and then, more slowly, start to increase. With regards to the model sketched in Fig. 1, we interpret these observations as LeTID defects first moving at a relatively high rate from the recombination-inactive state A to the recombination-active state B. Further, they move at a lower rate to the recombination-inactive state C. As we shall discuss in more detail below, these transitions, as well as their reverse reactions, happen simultaneously. The lifetime (and NDD) as a function of treatment time represents the superposition of all these transitions.

In two of the measurement series displayed in Fig. 3(a) (0.5 and 3 suns), the final lifetimes are slightly higher than the initial lifetimes. The lower initial than final lifetime, can be an indication that some defects are in the recombination-active state B already at the beginning of the presented measurement series or that other defects than LeTID might influencing the lifetime evolution of the samples during the illuminated annealing treatment.

Fig. 3(b) displays NDD calculated by (4) based on the lifetime data shown in Fig. 3(a), as well as least square optimization of the equation suggested by Vargas *et al.* [18] [see (6)] to these values.

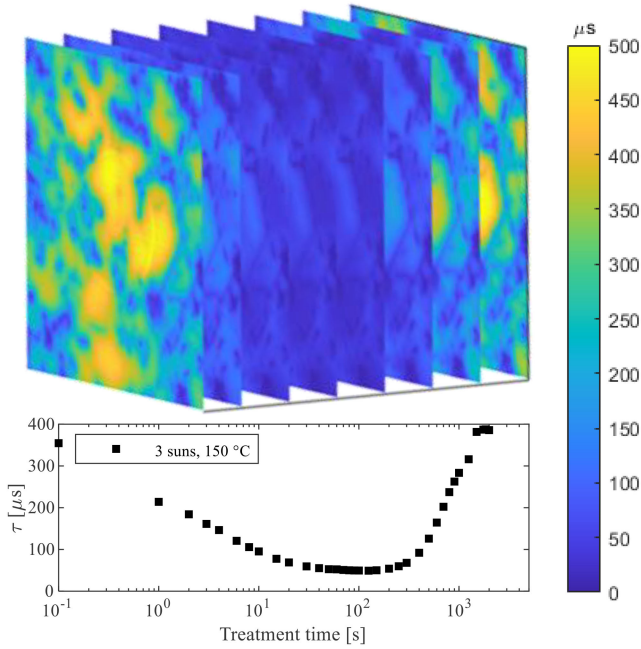


Fig. 4. Illustration showing the spatial features of our dataset. One PL image is acquired in each timestamp during the degradation and regeneration cycles.

The quality of the fit of (6) to our experimental data is, however, only moderately good. Especially, we notice an underestimation of the NDD at the beginning of the degradation process, and an overestimation later in the process. These suboptimalities indicate that the reaction rate has been underestimated early in the process (when the lifetime is high), while overestimated later in the process (when the lifetime is lower). Based on the sub-optimal fit in Fig. 3(b) and on literature stating the dependence of LeTID degradation and regeneration rate on excess carrier density [12], [16]–[18], we seek to improve (6) [18] by taking injection dependence into account in the equation.

B. Injection Dependence of Degradation and Regeneration Rates

In order to evaluate the dependence of the degradation and regeneration rate on charge carrier injection, we use a twofold approach. 1) We use measurement series acquired with different light intensities (0.5–3 suns) and accordingly, with different carrier injection level. 2) We utilize the fact that the lifetime (and thus also the injection level) varies internally in each of our samples because of their grain structure. At each timestamp during our degradation and regeneration cycles, a PL image is acquired (see Section II-C). We can therefore evaluate the degradation and regeneration behavior spatially across our samples. Fig. 4 illustrates the spatial features of our dataset. We calculate Δn from the lifetime maps, as the product of the local lifetime and the generation rate at the given illumination intensity. The injection dependence of the lifetime itself is not considered.

We use least square optimization in MATLAB R2020a to fit the equation suggested by Vargas *et al.* [18] [see (6)] to each pixel in our PL measurement series. Thereby, we obtain pixelwise

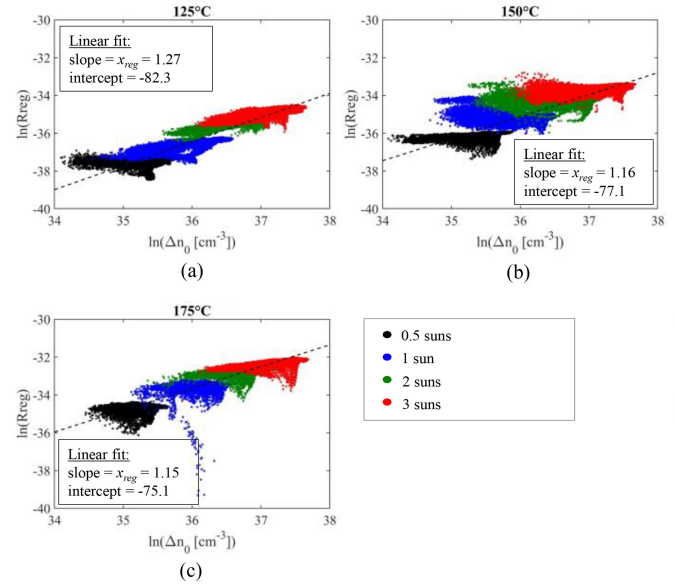


Fig. 5. Logarithmic dependence of R_{reg} on Δn_0 at 125 °C, 150 °C, and 175 °C. At each temperature, data from measurements at different illumination intensities are included.

values for degradation and regeneration rate ($R_{\text{deg/reg}}$) as well as for the maximum defect density (NDD_{max}) and for the factor A accounting for differences in NDD before and after the illumination and heat treatment (see Section I-B). Studying how these parameters vary spatially in relation to variations in the excess carrier density Δn help us understand how the degradation and regeneration rates depend on injection conditions.

Following (1), we assume that the rate R of a chemical reaction depend on the concentration of the reacting species. Considering excess carriers as a reacting species in the degradation and regeneration reactions, we have the relation

$$R_{\text{deg/reg}} = k'_{\text{deg/reg}} \cdot \Delta n^{x_{\text{deg/reg}}} \quad (7)$$

where Δn is the excess carrier concentration and x can be regarded as a stoichiometric coefficient for the excess carriers in the reaction. We have here applied the symbol k' , rather than k , to indicate that concentrations of other reacting species [e.g., P and Q in (1)] are not separated from the reaction rate constant. The number k' is therefore the *reaction rate coefficient with respect to excess carriers* and can vary with the concentration of other reacting species.

Taking the natural logarithm on both sides of (7), we get the relation

$$\ln(R_{\text{deg/reg}}) = \ln(k'_{\text{deg/reg}}) + x_{\text{deg/reg}} \cdot \ln(\Delta n) \quad (8)$$

indicating that the coefficient $x_{\text{deg/reg}}$ can be found as the slope of a log-log plot of Δn vs $R_{\text{deg/reg}}$. In Fig. 5, we study this relation for the regeneration process, i.e., for transition B \rightarrow C in Fig. 1.

The figure displays $\ln(R_{\text{reg}})$ for individual pixels plotted as a function of the logarithm of their initial injection level $\ln(\Delta n_0)$. Similar plots (not shown here) can be made with respect to the local Δn at other times than the starting time. As different

regions degrade at different rates, and therefore reach their most degraded state at different time, we have chosen the initial injection level Δn_0 as the least ambiguous value to apply in these plots. Data from measurement series at 125 °C, 150 °C, and 175 °C are included in separate plots in Fig. 5. Within each plot, data from measurements at different illumination intensities are included. As mc-Si samples may have regions where other recombination channels than the LeTID degradation dominates (e.g., recombination at dislocation clusters and grain boundaries), only 60% of the pixels with best fit within each temperature/illumination group were included in the figure. The quality of the fit was quantified by its mean square error (MSE). The limit of 60% was chosen because it gave a reasonable reduction of noise/outliers but seemed not to alter the main trends of the data.

Using a linear fit, we extract the slope of the included data [see dashed lines in Fig. 5(a)–(c)]. Within each temperature/illumination group we notice a trend which deviates slightly from the common trend at each temperature. Minimal change in R_{deg} is seen in for pixels that have differences in injection level caused by lifetime variations. At present, we have not identified the reason for this deviation. One possible explanation is a smearing effect (i.e., lateral diffusion of charge carriers) during the PL imaging which could lead to an underestimation of the regeneration rate in high lifetime regions and an overestimation in the low lifetime regions. Lateral diffusion of charge carriers during the light soaking, on the other hand, could lead to an underestimation of Δn in low lifetime regions and an overestimation of Δn in high lifetime regions. Both these effects would shift the slope within each temperature/illumination group slightly. As we cannot rule out these possibilities, we apply the slope of common linear fit dashed lines in Fig. 5(a)–(c) for further analyses. Following (7) and (8), this slope constitutes the stoichiometric coefficient x_{reg} for excess carriers in the regeneration reaction. Applying the relation in (7), we can then rewrite (6) as

$$\begin{aligned} \text{NDD}(t) = \text{NDD}_{\max} \{ & [1 - \exp(-R_{deg} * t)] \\ & - (1 + A) [1 - \exp(-k'_{reg} * \Delta n^{1.2} * t)] \}. \end{aligned} \quad (9)$$

For x_{reg} , we have here used the average value for the three temperatures in Fig. 5.

Having arrived at (9), in which the injection dependence of the *regeneration* rate is taken into account, we perform a new least square optimization to fit (9) to each pixel in our PL dataset. Thereby, we obtain an updated set of fitting parameters to each pixel of the images. Note that R_{reg} now is exchanged with $k'_{reg} \cdot \Delta n^{1.2}$, meaning that the fitting value that we obtain is the regeneration rate coefficient with respect to excess carriers k'_{reg} rather than the regeneration rate R_{reg} itself.

Following the same approach as for R_{reg} we can use the relation between the natural logarithm of R_{deg} and the natural logarithm of Δn to deduce a stoichiometric coefficient x_{deg} for Δn in the degradation process. Fig. 6 displays this relation at temperatures of 125 °C, 150 °C, and 175 °C. As in Fig 5, $\ln(R_{deg})$ is plotted as a function of the logarithm of the initial injection level $\ln(\Delta n_0)$. A similar plot in which $\ln(R_{deg})$ is plotted against

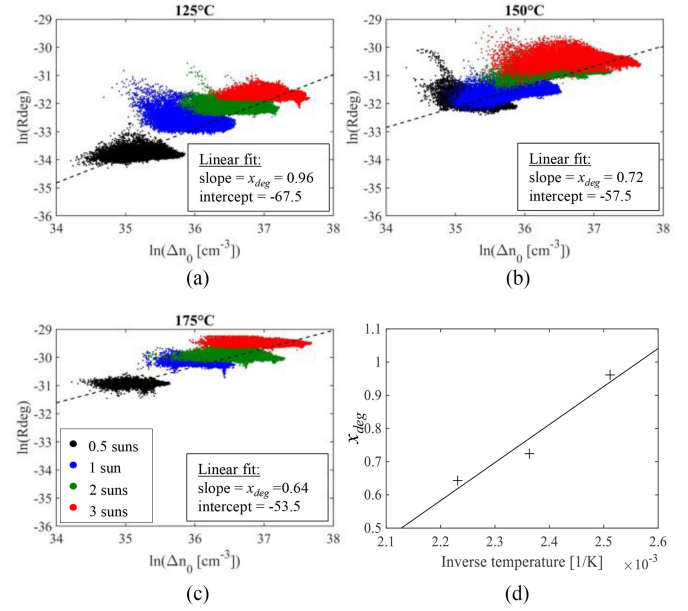


Fig. 6. (a)–(c) Logarithmic dependence of R_{deg} on Δn_0 at 125 °C, 150 °C, and 175 °C. (d) Linear dependence of x_{deg} on inverse temperature.

the logarithm of the most degrade injection level $\ln(\Delta n_{deg})$ is shown in the appendix for comparison. As in Fig. 5, the pixels are filtered according to the quality of the fit (quantified by the MSE), and only the 60% best are included. Again, we observe a deviation between the overall slope at each temperature (as indicated with dashed black lines) and the slope within each temperature/illumination group. For the same reasons as mentioned above for the regeneration rate, we chose to focus on the overall slope at each temperature for our further analyses.

Comparing the slopes of the linear fits in Fig. 6(a)–(c), we notice a decreasing trend with temperature. The observed temperature dependency indicates that we are looking at two simultaneous reactions, where neither can be neglected. The primary reaction we are studying is the transition $A \rightarrow B$ in Fig. 1. The data presented in Fig. 6, however, suggest that the backward reaction (transition $B \rightarrow A$) also must be taken into consideration. Influence of regeneration (transition $B \rightarrow C$), which must be expected at the present experimental conditions [15], has already been accounted for by the regeneration term in (9). Hence, we do not expect influence of this transition in the degradation data shown in Fig. 6.

The temperature dependence of x_{deg} displayed in Fig. 6 indicate that the forward ($A \rightarrow B$) and backward ($B \rightarrow A$) transitions under consideration have different activation energies and also different dependency on excess electrons Δn . The individual temperature and injection dependence of these transitions cannot be separated under the current experimental conditions. As a simplification, the combined temperature dependencies of these reactions are collected in the variable $x_{deg}(T)$. This variable is here defined by a linearization of the x_{deg} values in Fig. 6(a)–(c) plotted against the corresponding inverse temperature [see Fig. 6(d)]. Our updated equation for the development of the

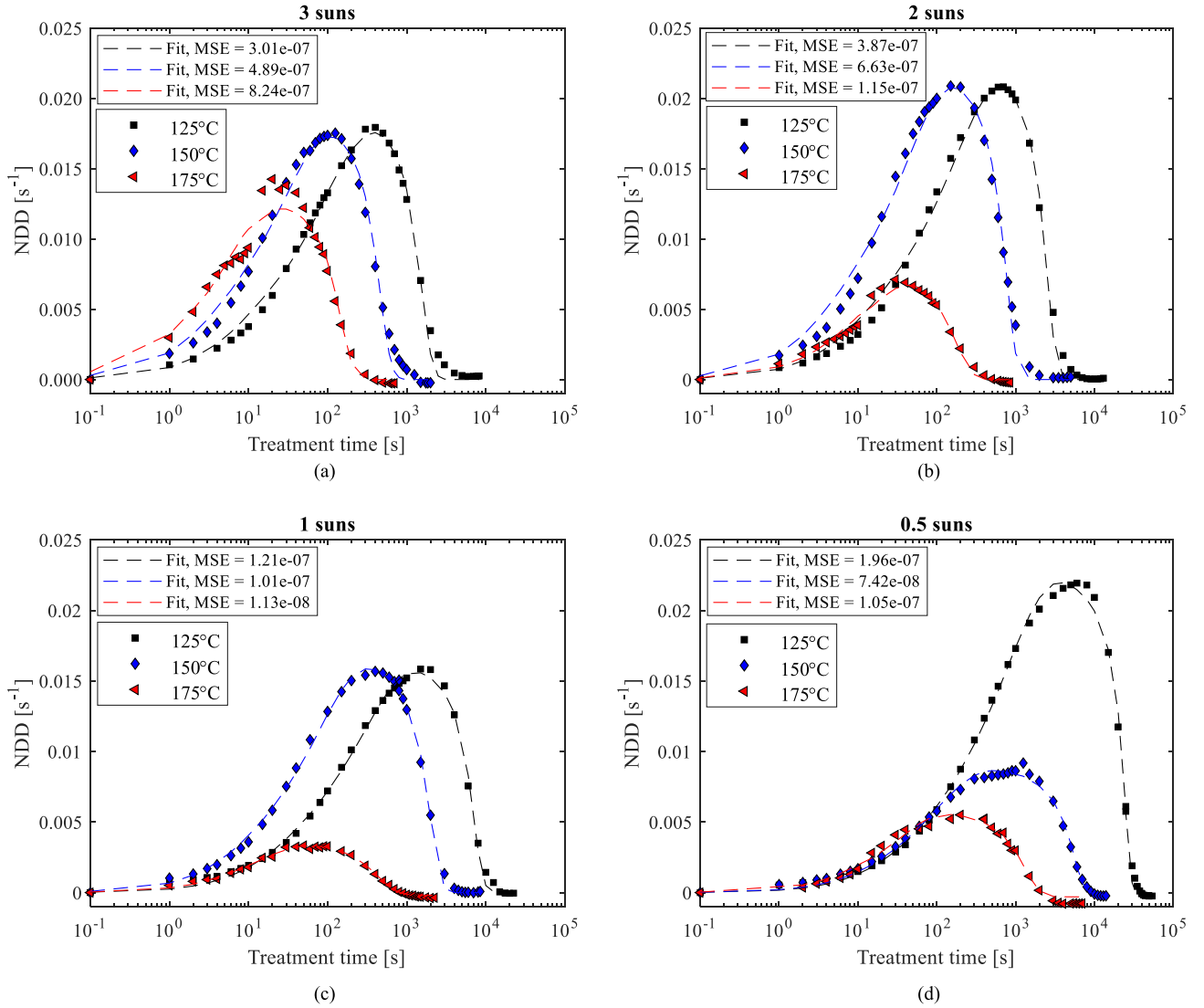


Fig. 7. Evolution of NDD as a function of treatment time at various illumination intensities and temperatures. The NDD values are calculated as an average of the central region in the PL images, corresponding to the QSSPC measurement coil. The dashed lines represent the least square fit of (10) to the experimental data.

NDD(t) then becomes

$$\text{NDD}(t) = \text{NDD}_{\max} \left\{ \left[1 - \exp \left(-k'_{\text{deg}} * \Delta n^{x_{\text{deg}}(T)} * t \right) \right] - (1 + A) \left[1 - \exp \left(-k'_{\text{reg}} * \Delta n^{1.2} * t \right) \right] \right\} \quad (10)$$

where k'_{deg} is the degradations rate coefficient with respect to excess carriers and the exponent and $x_{\text{deg}}(T)$ is a function of inverse temperature given by the linearization in Fig. 6(d). The experimental data from which $x_{\text{deg}}(T)$ here is determined from a relatively narrow temperature range (125°C–175°C). More experimental data are needed to determine the dependence of x_{deg} on T in a larger temperature range. For the regeneration reaction, with an insignificant temperature dependence of x_{reg} in the investigated temperature range [see Fig. 5(a)–(c)], we assume that the forward reaction from B \rightarrow C dominates. The

backwards reaction (transition C \rightarrow B) seems not, or only to a low extent, to take place at these conditions.

In both Figs. 5 and 6, we notice that the intercept of the fitted line with the y-axis increase with temperature. Following (8), this intercept represents the natural logarithm of $k'_{\text{deg/reg}}$. As these reaction rate constants are a functions of temperature [via Arrhenius equation, (2)], it is expected that also the number $\ln(k'_{\text{deg/reg}})$ varies with temperature.

Using the updated expression in (10), we obtain a drastically improved fit to our experimental data, as compared with (6) used by Vargas *et al.* [18]. Fig. 7 shows the evolution of NDD as a function of treatment time at various illumination intensities and temperatures along with the least square fit of (10) to the experimental data. Comparison with Fig. 3(b) shows a clear improvement of the fitting quality, as quantified by MSE.

The quantity $x_{\text{deg}}(T)$ introduced in (10) can be described as the temperature dependence of the injection dependence of the observed degradation. As the observed degradation is the

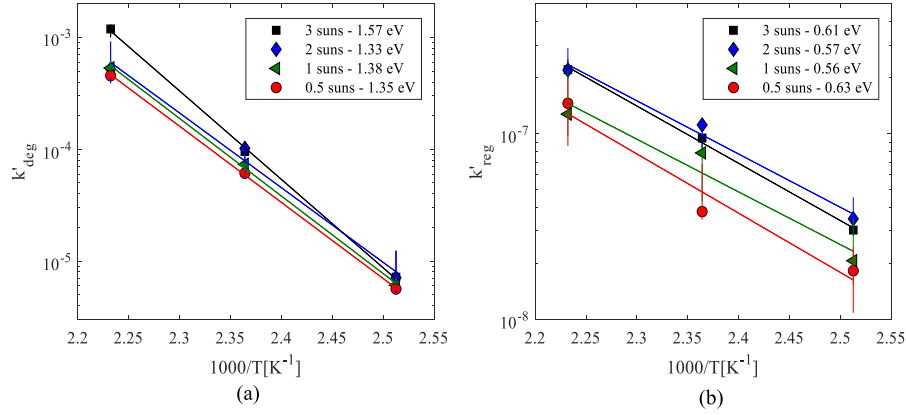


Fig. 8. Degradation (a) and regeneration (b) rate constants of samples subjected to different illumination intensities and temperatures as function of inverse temperature. The rate coefficients are estimated by fitting experimental data to the updated equation that we arrive at within this work [see (10)] (see main text). The error bars indicate the uncertainty related to the Arrhenius fit.

superposition of the transitions $A \rightarrow B$ and $B \rightarrow A$, $x_{\text{deg}}(T)$ describes the temperature dependence of the injection dependence of the sum of these reactions. Our values for $x_{\text{deg}}(T)$ varying in the range 0.64–0.96 [see Fig. 6(a)–(c)], agree well with the previously reported value 0.86 ± 0.08 by Kwopil *et al.* [16] for the corresponding injection dependence of the degradation reaction.

Our values for $x_{\text{deg}}(T)$ increase with decreasing temperature. Moreover, within the investigated temperature range (125 °C–175 °C), they seem to approach unity when the temperature decreases. This could indicate that at relatively low temperatures the $A \rightarrow B$ transition dominates, and moreover that the limiting step in this transition involves one electron [16]. The decreasing $x_{\text{deg}}(T)$ at higher temperatures, can be interpreted as an increased influence of the $B \rightarrow A$ transition.

C. Activation Energies of the Degradation and Regeneration Reactions

Table I displays values for the activation energy of the degradation and regeneration process reported in the literature, along with values obtained in this work. Two sets of values from this work are reported. The first set is calculated from reaction rates $R_{\text{deg/reg}}$ fitted according to (6) introduced by Vargas *et al.* [18]. The second set is calculated from values for $k'_{\text{deg/reg}}$ fitted according to (10), taking the injection dependence of R_{deg} and R_{reg} into account. The Arrhenius fits (2) of k'_{reg} and k'_{deg} to inverse temperature are shown in Fig. 8.

Both in the case of degradation and regeneration, our first set of activation energies based on (6) fall well within the range of activation energies already reported in the literature. Our second set of activation energies accounting for the injection dependence of the reaction rate [see (10)] show discrepancies from most of the literature values. The discrepancy is expected since the values are calculated based on different criteria. Moreover, the activation energies obtained from fitting to (10) are, within the frame of our uncertainties, not depending on illumination intensity. This is also expected, as the injection level which is directly linked to the illumination intensity is separated from the reaction rate constant and $k'_{\text{deg/reg}}$ in our calculations.

Among the references listed in Table I, there is only one work (Graf *et al.* [40]) in which the injection dependence of the degradation and regeneration rates is taken into account. These authors used varied light intensity to ensure a constant injection level despite the change in carrier lifetime during degradation and regeneration of their samples. In the other listed works [6], [18], [27], [41]–[44] the effect of evolving lifetime on excess carrier density for a fixed generation rate is ignored in the applied fitting procedures. Instead, kinetic constants are derived without correction for changing injection level. This weakness has recently also been mentioned by Repins *et al.* [45]. The values for activation energy of regeneration $E_{a,\text{reg}}$ that we obtain from fitting to (10), i.e., by taking injection dependence into account mathematically, deviates from the values reported in these works [6], [18], [27], [41]–[44], but correspond very well to the value reported by Graf *et al.* [40], taking injection dependence in account by experimental modifications. The good correspondence between our result and the result by Graf *et al.* [40] can be interpreted as a confirmation of the applied fitting procedure, underpinning the importance of taking the evolution of charge carrier injection into account in the evaluation of LeTID kinetics.

The values for activation energy of degradation $E_{a,\text{deg}}$ that we obtain from fitting to (10), is higher than all the other values for $E_{a,\text{deg}}$ listed in Table I. This discrepancy may be a result of the inclusion of a temperature dependent exponent $x_{\text{deg}}(T)$, as shown in Fig. 6(d), in the degradation term of (10). We propose that the equilibrium of the $A \rightleftharpoons B$ reaction, and therefore also the injection level dependence of the reaction rate depends on the temperature. Our reported activation energy differs from literature values as we extract the injection level and its temperature dependence, prior to determining the activation energy for the degradation. Strictly speaking, an activation energy relates to only one single chemical reaction. As the value we report here is estimated based on the equilibrium between two simultaneous reactions, it would be more correctly described by the term *apparent activation energy*.

It is interesting to note that the previously reported values that are closest to those we obtain, are those reported by Vargas *et al.*

TABLE I
ACTIVATION ENERGIES FOR DEGRADATION AND REGENERATION OF THE LETID DEFECT, AS REPORTED IN THE LITERATURE;
VALUES ESTIMATED IN THIS WORK ARE INCLUDED

Reference	Wafer/ cells	ρ [$\Omega\text{-cm}$]	T range [$^{\circ}\text{C}$]	Measurement method	Fitting method	$E_{a,\text{deg}}$ [eV]	$E_{a,\text{reg}}$ [eV]	Illumination [kW/m^2]
Zhou et al.[41]	p-type cast mono PERC	2	150-250	Suns-Voc	“exponential function with one growth phase and one decay phase”	0.65 ± 0.05	0.80 ± 0.04	7 (LED)
Liu et al.[42]	p-type mc	1.7	100-300	QSS-PC	“single-exponential fit - (the plateaued region was neglected during the fitting)”	0.78 ± 0.05 0.64 ± 0.04 0.63 ± 0.11 0.62 ± 0.07 0.62 ± 0.09	0.70 ± 0.04 0.67 ± 0.02 0.68 ± 0.02 0.72 ± 0.03 0.78 ± 0.08	14.5 (laser) 30.5 (laser) 44.9 (laser) 60.1 (laser) 74.5 (laser)
Yao et al.[43]	p-type mc	0.82 1.06 1.13 1.22 1.33	134-176	QSS-PC	Eq.(6)	0.76 ± 0.09 0.74 ± 0.08 0.84 ± 0.07 0.87 ± 0.10 0.92 ± 0.09	0.78 ± 0.11 0.77 ± 0.13 0.92 ± 0.15 0.90 ± 0.10 0.92 ± 0.07	45 (laser)
Bredemeier et al.[27]	p-type mc	1.7	75-120	QSS-PC	*	0.89 ± 0.04 (fast) 0.94 ± 0.06 (slow)		0.5 (halogen)
Vargas et al.[18]	p-type mc	1.7	138-275	QSS-PC	Eq.(6)	1.08 ± 0.05	1.11 ± 0.04	DA
Vargas et al.[44]	n-type mc	4.6	100-175			1.23 ± 0.16	1.34 ± 0.08	DA
Chen et al.[6]	n-type Cz	2	140-175	QSS-PC	**	0.76 ± 0.02 0.70 ± 0.05	0.97 ± 0.05 0.83 ± 0.04	DA 0.02 (halogen)
Graf et al. [40]	p-type FZ	1.5	80-150	QSS-PC	“double exponential fit”	0.78 ± 0.09	0.62 ± 0.09	~1 (laser) Intensity adjusted to keep Δn constant
Current work	p-type mc	0.7	125-175	PL	Eq.(6)	0.94 ± 0.19 0.82 ± 0.09 0.71 ± 0.07 0.71 ± 0.07	0.86 ± 0.10 0.91 ± 0.10 0.84 ± 0.08 0.77 ± 0.08	0.5 1 2 3
						1.35 ± 0.14 1.38 ± 0.14 1.33 ± 0.31 1.57 ± 0.17	0.63 ± 0.12 0.56 ± 0.12 0.57 ± 0.07 0.61 ± 0.06	0.5 1 2 3
				PL	Eq.(10)			

* $\text{NDD}(t) = a(1 - \exp(-R_{\text{deg,fast}} \cdot t)) + b(1 - \exp(-R_{\text{deg,slow}} \cdot t))$.

** $\text{NDD}(t) = \text{NDD}_{\text{bulk}} \{ [f_{\text{fast}}(1 - \exp(-R_{\text{deg,fast}} \cdot t))] + [f_{\text{slow}}(1 - \exp(-R_{\text{deg,slow}} \cdot t))] + [\exp(-R_{\text{deg}}t) - 1] \} + \text{NDD}_{\text{bulk}}(1 - \exp(-R_{\text{SRD}}t))$.

Where f_{fast} and f_{slow} are the proportion of defects pertaining to two observed degradation reactions (a fast-forming and a slow forming). R_{SRD} is the rate of surface-related degradation.

[18], [44] for DA, i.e., for degradation without carrier injection. Considering that evolving carrier injection might influence the other reported results [6], [27], [41]–[43], whereas it has been accounted for (and hence should not influence the result) in our fitting to (10), it is reasonable that our result are closer to those found for degradation without carrier injection. The latter holds true, of course, only upon the assumption that DA and LeTID is indeed evoking the same degradation reaction.

We expect some impact of from BO-related degradation in our HPMC-Si samples [24], [25]. Therefore, we cannot rule out the possibility that the degradation rates at some temperatures, and hence, the estimated activation energy is influenced by the presence of BO-defects. The investigations by Graf *et al.* [40], in which evolving carrier injection is accounted for experimentally, were done using FZ-Si, in which no impact of BO-LID is expected.

None of the values for activation energy listed in Table I, neither those published by others [6], [18], [27], [40]–[44], nor those arrived at in this work, takes the evolution in the concentration of the reacting species (A and C, see Fig. 1) into account in their

derivation of the reaction rates and activation energies. The rate of a reaction is a function of the reaction rate coefficient k and of the reactants concentrations [see (1)]. These concentrations vary over the course of a reaction. Finding the true activation energy and attempt frequency of a reaction, therefore requires separating the reaction rate coefficient k from the other quantities contributing to reaction rate R . Since the chemical identity of the LeTID defect as well as its reaction pattern with other species and with excess electrons are unknown, this is currently not possible. Both (6) and (10) assume a first-order reaction with respect to B.

D. Spatial Evaluation of Degradation and Regeneration Parameters

Fitting the updated equation in (10) to each pixel in our PL-image series, gives spatially resolved maps of the degradation and regeneration parameters k'_{deg} , k'_{reg} , and NDD_{max} at different combinations of temperature and illumination. As an example, we have chosen the maps for degradation at 150°C

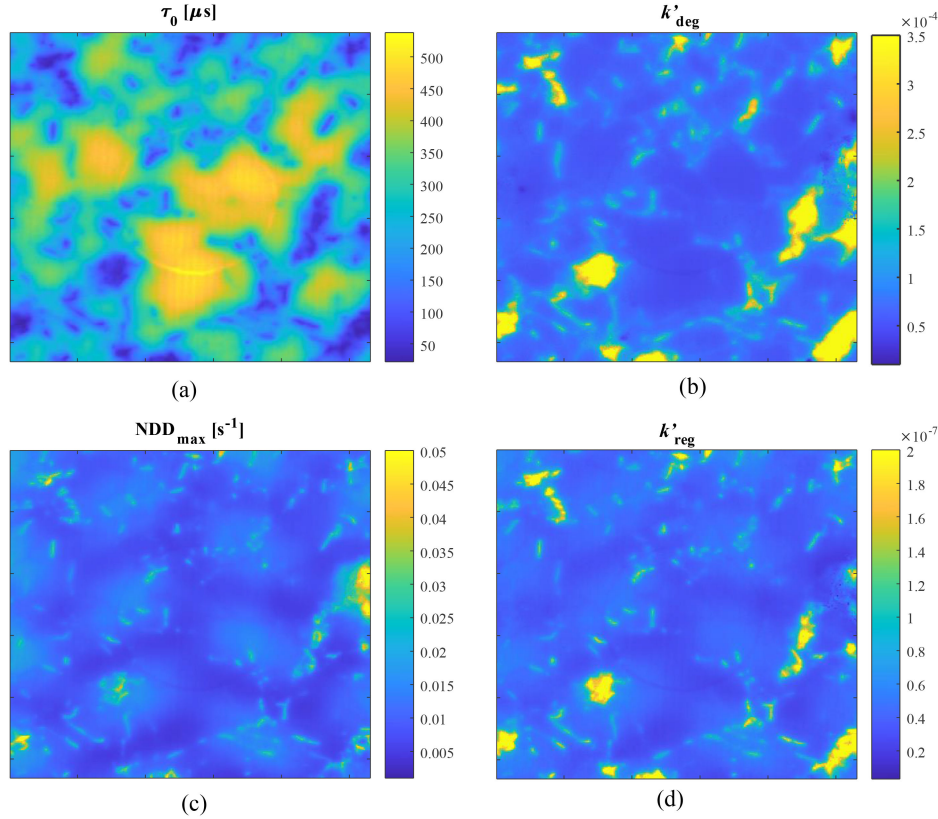


Fig. 9. Spatially resolved maps of initial lifetime (τ_0), k'_{deg} , k'_{reg} , and NDD_{max} by degradation at 150 °C and 0.5 suns illumination. Each pixel in the maps is fitted with least square optimization to (10).

and 0.5 suns shown Fig. 9(b)–(d). A map of the initial lifetime τ_0 for the same sample is shown in Fig. 9(a) for comparison.

The map of NDD_{max} [see Fig. 9(c)] possesses a grid-like pattern which we recognize as the pattern from the conveyor belt carrying the samples during the firing process. This observation, which clearly is in line with previous reports by Niewelt *et al.* [32] and by Selinger *et al.* [26], indicate that the maximum degradation depend strongly on the local temperature profile during the contact firing process. We assume that the regions that have been in contact with the conveyor belt (i.e., the regions having a smaller NDD_{max}) have seen a slower temperature ramp during cooling compared with the regions not being in contact with the belt.

Fig. 9(c) further indicates that large values of NDD_{max} appear in regions that initially possess a low charge carrier lifetime, either because of dislocation clusters or grain boundaries. This observation corresponds well to previous reports by Skorka *et al.* [21] and by Krauss *et al.* [46] reporting a more severe LeTID degradation in such regions. The degradation and regeneration rate constants [see Fig. 9(b) and (d)] also show a clear anti-correlation to the initial lifetime. Within high lifetime regions, the degradation and regeneration rates are largely constant. However, even the grain boundaries that are well hydrogen passivated, and not visible in the lifetime map, become visible as lighter features in the map of the degradation rate coefficient [see Fig. 9(b)] and darker features in the map of the regeneration rate coefficient [see Fig. 9(d)]. Interestingly, the pattern from the

conveyor belt is also visible in the map of the regeneration rate coefficient [see Fig. 9(d)]. This observation can be directly linked to the higher concentration of recombination active defects (N_B) in these regions. From (1), we expect the rate of a transition (in this case the transition $B \rightarrow C$) to increase with the concentration of the reacting species.

IV. SUMMARY

The lifetime evolution of HPMC-Si sister wafers showing degradation and subsequent regeneration when subjected to illuminated annealing has been studied. We extract the injection level dependence from the reaction rate coefficients and propose an updated equation for LeTID degradation and regeneration in which the evolving charge carrier concentration is considered. Applying the new equation, we obtain a drastically improved fit to our experimental data. For the regeneration process, we find a stoichiometric coefficient of 1.2 for excess charge carriers. For the degradation process, we find that the stoichiometric coefficient for excess charge carriers approach unity at decreasing temperatures.

The observed evolution of normalised defect density throughout a degradation and regeneration cycle of a sample must be considered as the superposition of forward and backward transitions between states A, B, and C (see Fig. 1). With our updated equation, taking the influence of evolving charge carrier density on each of these transitions into account, we arrive at

activation energies of $E_{a,deg} = 1.38 \pm 0.14$ eV and $E_{a,reg} = 0.56 \pm 0.12$ eV for the degradation and regeneration process, respectively. These values differ from most values reported in the literature as we extract the injection level and its temperature dependence, prior to determining the activation energy.

APPENDIX

Fig. A.1 shows the Δn dependent lifetime curves for one selected sample in its initial, degraded and regenerated state. Typically, the recovered lifetime curve is quite similar to the corresponding initial curve.

Fig. A.2 shows $\ln(R_{deg})$ plotted as function of the local carrier injection level at the most degraded state. The most degraded state is here defined as the timestamp where the average lifetime within each respective wafer is the least.

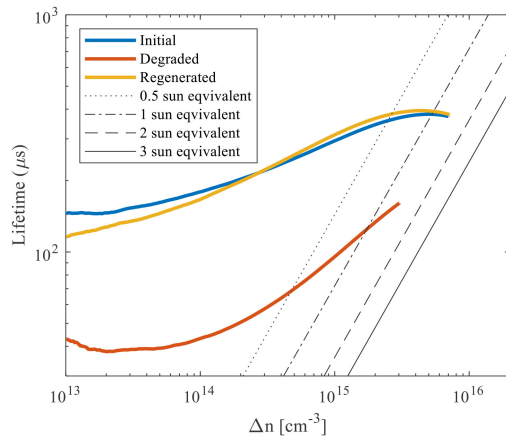


Fig. A.1. Injection dependent lifetime of the wafer degraded at 150 °C and with 1 Sun illumination in its initial, degraded and regenerated state. Additionally, equivalent lifetime curves for 0.5, 1, 2, and 3 suns are shown.

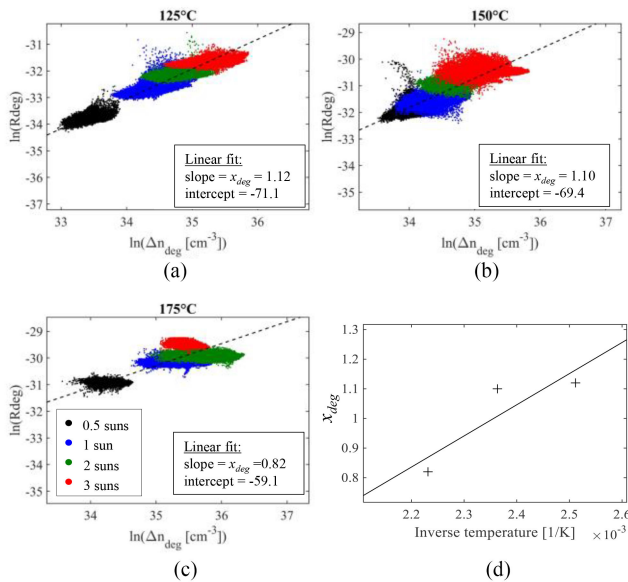


Fig. A.2. Logarithmic dependence of R_{deg} on Δn the point of the time when each sample on average is most degraded.

ACKNOWLEDGMENT

The data that support the findings of this study are available from the corresponding author upon reasonable request.

REFERENCES

- [1] F. Kersten *et al.*, "Degradation of multicrystalline silicon solar cells and modules after illumination at elevated temperature," *Sol. Energy Mater. Sol. Cells*, vol. 142, pp. 83–86, 2015.
- [2] K. Ramspeck *et al.*, "Light induced degradation of rear passivated mc-Si solar cells," in *Proc. 27th Eur. Photovoltaic Sol. Energy Conf. Exhib.*, 2012, pp. 861–865.
- [3] M. A. Jensen *et al.*, "Evaluating root cause: The distinct roles of hydrogen and firing in activating light- and elevated temperature-induced degradation," *J. Appl. Phys.*, vol. 124, no. 1–8, 2018, Art. no. 085701.
- [4] A. Ciesla *et al.*, "Hydrogen-induced degradation," in *Proc. 7th World Conf. Photovolt. Energy Convers.*, 2018, pp. 1–8.
- [5] D. Bredemeier, D. C. Walter, and J. Schmidt, "Lifetime degradation in multicrystalline silicon under illumination at elevated temperature: Indications for the involvement of hydrogen," *AIP Conf. Proc.*, vol. 1999, 2018, Art. no. 130001.
- [6] D. Chen *et al.*, "Hydrogen-induced degradation: Explaining the mechanism behind light- and elevated temperature-induced degradation in n- and p-type silicon," *Sol. Energy Mater. Sol. Cells*, vol. 207, 2020, Art. no. 110353.
- [7] D. Bredemeier, D. C. Walter, and J. Schmidt, "Possible candidates for impurities in mc-Si wafers responsible for light-induced lifetime degradation and regeneration," *Sol. RRL*, vol. 2, pp. 1–5, 2018.
- [8] R. Sharma, S. Vajandar, T. Osipowicz, J. B. Li, A. G. Aberle, and Y. Huang, "Hydrogen diffusion from PECVD silicon nitride into multicrystalline silicon wafers: Elastic recoil detection analysis (ERDA) measurements and impact on light and elevated temperature induced degradation (LETID)," *AIP Conf. Proc.*, vol. 2147, 2019, Art. no. 140009.
- [9] J. Schmidt, D. Bredemeier, and D. C. Walter, "On the defect physics behind light and elevated temperature-induced degradation (LeTID) of multicrystalline silicon solar cells," *IEEE J. Photovolt.*, vol. 9, no. 6, pp. 1497–1503, Nov. 2019.
- [10] R. Eberle, W. Kwapil, F. Schindler, S. W. Glunz, and M. C. Schubert, "Firing temperature profile impact on light induced degradation in multicrystalline silicon," *Energy Procedia*, vol. 124, pp. 712–717, 2017.
- [11] K. Kraus, A. A. Brand, F. Fertig, S. Rein, and J. Nekarda, "Fast regeneration processes to avoid light-induced degradation in multicrystalline silicon solar cells," *IEEE J. Photovolt.*, vol. 6, no. 6, pp. 1427–1431, Nov. 2016.
- [12] T. H. Fung *et al.*, "A four-state kinetic model for the carrier-induced degradation in multicrystalline silicon: Introducing the reservoir state," *Sol. Energy Mater. Sol. Cells*, vol. 184, pp. 48–56, 2018.
- [13] T. Luka, M. Turek, and C. Hagendorf, "Defect formation under high temperature dark-annealing compared to elevated temperature light soaking," *Sol. Energy Mater. Sol. Cells*, vol. 187, pp. 194–198, 2018.
- [14] H. C. Sio, D. Kang, X. Zhang, J. Yang, J. Jin, and D. MacDonald, "The role of dark annealing in light and elevated temperature induced degradation in p-Type mono-like silicon," *IEEE J. Photovolt.*, vol. 10, no. 4, pp. 992–1000, Jul. 2020.
- [15] W. Kwapil, J. Schon, T. Niewelt, and M. C. Schubert, "Temporary recovery of the defect responsible for Light- and Elevated temperature-induced degradation: Insights into the physical mechanisms behind LeTID," *IEEE J. Photovolt.*, vol. 10, no. 6, pp. 1–13, Nov. 2020.
- [16] W. Kwapil, T. Niewelt, and M. C. Schubert, "Kinetics of carrier-induced degradation at elevated temperature in multicrystalline silicon solar cells," *Sol. Energy Mater. Sol. Cells*, vol. 173, pp. 80–84, 2017.
- [17] D. Chen *et al.*, "Evidence of an identical firing-activated carrier-induced defect in monocrystalline and multicrystalline silicon," *Sol. Energy Mater. Sol. Cells*, vol. 172, pp. 293–300, 2017.
- [18] C. Vargas, G. Coletti, C. Chan, D. Payne, and Z. Hameiri, "On the impact of dark annealing and room temperature illumination on p-type multicrystalline silicon wafers," *Sol. Energy Mater. Sol. Cells*, vol. 189, pp. 166–174, 2019.
- [19] C. E. Chan *et al.*, "Rapid stabilization of high-performance multicrystalline P-type silicon PERC cells," *IEEE J. Photovolt.*, vol. 6, no. 6, pp. 1473–1479, Nov. 2016.
- [20] C. E. Chan *et al.*, "Modulation of carrier-induced defect kinetics in multicrystalline silicon PERC cells through dark annealing," *Sol. RRL*, vol. 1, no. 2, Feb. 2017, Art. no. 1600028.

- [21] D. Skorka, A. Zuschlag, and G. Hahn, "Spatially resolved degradation and regeneration kinetics in mc-Si," in *Proc. 32nd Eur. Photovolt. Sol. Energy Conf. Exhib.*, München, Germany, 2016, pp. 643–646.
- [22] W. Kwapil, J. Dalke, T. Niewelt, and M. C. Schubert, "LeTID and (extended) Bo-related degradation and regeneration in B- and Ga-doped monocrystalline silicon during dark and illuminated anneals," in *Proc. 37th Eur. PV Sol. Energy Conf. Exhib.*, 2020, pp. 1–4.
- [23] S. W. Glunz, S. Rein, J. Y. Lee, and W. Warta, "Minority carrier lifetime degradation in boron-doped Czochralski silicon," *J. Appl. Phys.*, vol. 90, no. 5, pp. 2397–2404, 2001.
- [24] R. Søndenå, H. Haug, C. C. You, J. Zhu, and M. S. Wiig, "Evolution of defect densities with height in a HPMC-SI ingot," *AIP Conf. Proc.*, vol. 2147, 2019, Art. no. 140010.
- [25] R. Søndenå and M. S. Wiig, "Evolution of the light sensitive defects in high performance multicrystalline silicon wafers," *Phys. J. Appl.*, vol. 125, 2019, Art. no. 085701.
- [26] M. Selinger *et al.*, "Spatially resolved analysis of light induced degradation of multicrystalline PERC solar cells," *Energy Procedia*, vol. 92, pp. 867–872, 2016.
- [27] D. Bredemeier, D. Walter, and J. Schmidt, "Light-induced lifetime degradation in high-performance multicrystalline silicon: Detailed kinetics of the defect activation," *Sol. Energy Mater. Sol. Cells*, vol. 173, pp. 2–5, 2017.
- [28] T. Niewelt, J. Schön, F. Schindler, and M. C. Schubert, "Understanding the light - induced degradation at elevated temperatures: Similarities between multicrystalline and floatzone p - type silicon," *Prog. Photovolt.*, vol. 26, pp. 533–542, 2018.
- [29] T. Luka, M. Turek, C. Kranert, S. Großer, and C. Hagendorf, "Microstructural investigation of LID sensitive mc-PERC solar cells," *Energy Procedia*, vol. 124, pp. 759–766, 2017.
- [30] T. Luka, S. Großer, C. Hagendorf, K. Ramspeck, and M. Turek, "Intra-grain versus grain boundary degradation due to illumination and annealing behavior of multi-crystalline solar cells," *Sol. Energy Mater. Sol. Cells*, vol. 158, pp. 43–49, 2016.
- [31] J. Lindroos, A. Zuschlag, J. Carstensen, and G. Hahn, "Light-induced degradation variation in industrial multicrystalline PERC silicon solar cells," *AIP Conf. Proc.*, vol. 1999, 2018, Art. no. 130013.
- [32] T. Niewelt, R. Post, F. Schindler, W. Kwapil, and M. C. Schubert, "Investigation of LeTID where we can control it—Application of FZ silicon for defect studies," *AIP Conf. Proc.*, vol. 2147, 2019, Art. no. 1400061.
- [33] D. Bredemeier, D. Walter, S. Herlufsen, and J. Schmidt, "Understanding the light-induced lifetime degradation and regeneration in multicrystalline silicon," *Energy Procedia*, vol. 92, pp. 773–778, 2016.
- [34] K. Nakayashiki *et al.*, "Engineering solutions and root-cause analysis for light-induced degradation in p-Type multicrystalline silicon PERC modules," *IEEE J. Photovolt.*, vol. 6, no. 4, pp. 860–868, Jul. 2016.
- [35] T. Niewelt, M. Selinger, N. E. Grant, W. Kwapil, J. D. Murphy, and M. C. Schubert, "Light-induced activation and deactivation of bulk defects in boron-doped float-zone silicon," *J. Appl. Phys.*, vol. 121, no. 18, 2017, Art. no. 185702.
- [36] D. Bredemeier, D. Walter, S. Herlufsen, and J. Schmidt, "Lifetime degradation and regeneration in multicrystalline silicon under illumination at elevated temperature," *AIP Adv.*, vol. 6, 2016, Art. no. 035119.
- [37] U. Varshney *et al.*, "Impact of substrate thickness on the degradation in multicrystalline silicon," *IEEE J. Photovolt.*, vol. 11, no. 1, pp. 65–72, Jan. 2021.
- [38] H. Haug, R. Søndenå, M. S. Wiig, and E. S. Marstein, "Temperature dependent photoluminescence imaging calibrated by photoconductance measurements," *Energy Procedia*, vol. 124, pp. 47–52, 2017.
- [39] P. M. Weiser, E. Monakhov, H. Haug, M. S. Wiig, and R. Søndenå, "Hydrogen-related defects measured by infrared spectroscopy in multicrystalline silicon wafers throughout an illuminated annealing process," *J. Appl. Phys.*, vol. 127, no. 6, 2020, Art. no. 065703.
- [40] A. Graf, A. Herguth, and G. Hahn, "Determination of BO-LID and LeTID related activation energies in Cz-Si and FZ-Si using constant injection conditions," *AIP Conf. Proc.*, vol. 2147, 2019, Art. no. 140003.
- [41] C. Zhou, F. Ji, S. Cheng, J. Zhu, W. Wang, and D. Hu, "Light and elevated temperature induced degradation in B–Ga co-doped cast mono Si PERC solar cells," *Sol. Energy Mater. Sol. Cells*, vol. 211, 2020, Art. no. 110508.
- [42] S. Liu *et al.*, "Investigation of temperature and illumination dependencies of carrier-induced degradation in p-type multi-crystalline silicon," *AIP Conf. Proc.*, vol. 1999, no. 1, 2018, Art. no. 130014.
- [43] Z. Yao, D. Zhang, J. Wu, F. Jiang, G. Xing, and X. Su, "Evolution of LeTID defects in industrial multi-crystalline silicon wafers under laser illumination—Dependency of wafer position in brick and temperature," *Sol. Energy Mater. Sol. Cells*, vol. 218, 2020, Art. no. 110735.
- [44] C. Vargas *et al.*, "Degradation and recovery of n-Type multi-crystalline silicon under illuminated and dark annealing conditions at moderate temperatures," *IEEE J. Photovolt.*, vol. 9, no. 2, pp. 355–363, Mar. 2019.
- [45] I. L. Repins, F. Kersten, B. Hallam, K. VanSant, and M. B. Koentopp, "Stabilization of light-induced effects in Si modules for IEC 61215 design qualification," *Sol. Energy*, vol. 208, pp. 894–904, 2020.
- [46] K. Krauss, F. Fertig, D. Menzel, and S. Rein, "Light-induced degradation of silicon solar cells with aluminium oxide passivated rear side," *Energy Procedia*, vol. 77, pp. 599–606, 2015.